Investigation of failure initiation in curved composite laminates using a higher-order beam model

C. Thurnherr[a,*], R.M.J. Groh[b,*], P. Ermanni[a], P.M. Weaver[b]

[a] *Laboratory of Composite Materials and Adaptive Structures, Department of Mechanical and Process Engineering, ETH Zürich, Tannenstr. 3, CH-8092 Zürich, Switzerland*

[b] *Advanced Composites Centre for Innovation and Science, University of Bristol, Queen's Building, University Walk, Bristol, BS8 1TR, UK*

Abstract

Curved laminates are prone to delamination failure from applied bending moments that straighten out the laminate and induce tensile stresses in the unreinforced radial direction. These non-classical through-thickness stresses are important even for thinner configurations and need to be accounted for in the design of lightweight composite structures, preferably in a computationally efficient manner. Here, we investigate failure-inducing critical stresses for a number of curved laminates using a higher-order beam model derived from the Hellinger-Reissner mixed variational principle, which guarantees that the hoop, interlaminar shear and radial stresses are equilibrated. By solving the governing equations of the theory in the strong form using the pseudo-spectral differential quadrature method, the model is capable of predicting accurate 3D stress fields in curved laminates, even in the vicinity of loacalised features such as supported edges. The model is used alongside commonly used failure criteria to reproduce experimental failure initiation results found in the literature, and the comparison suggests that failure mode, location and load are all predicted accurately. Finally, failure maps that highlight the critical stress component for failure initiation are constructed. As the thickness of the curved laminate increases, the critical stress component transitions from intralaminar hoop stress to interlaminar shear or radial stress depending on the specific laminate configuration. These findings and failure maps collectively provide insights into the mechanics of failure initiation that should also prove useful for design purposes.

Keywords: Curved laminates, higher-order modeling, interlaminar stresses, anisotropic materials, damage onset

1. Introduction

Due to their high specific strength and stiffness the predominance of composite materials in primary load-bearing aircraft structures is on the rise. In curved laminates, such as T-shaped stringers on aircraft wings, interlaminar stresses arise even for thin wall-thicknesses when the curved geometry is straightened and these interlaminar stresses are known drivers of delamination onset [1, 2]. To account for delamination failure as early as possible in the design process, analytical tools that accurately predict the stress fields in a computationally efficient manner are key [3, 4, 5].

To date, the investigation of failure initiation and certification of load-bearing aircraft structures requires detailed experimental validation from the coupon to the assembly level. Hence, examples of experimental studies on failure initiation in curved laminates are plentiful. Wimmer et al. [6] studied the failure initiation and propagation in L-shaped laminates experimentally and numerically. Hao et al. [7] conducted experiments to investigate delamination in different laminates. Michel et al. [8] analyzed curved laminates in four-point bending tests. Sun et al. [9] investigated failure loads and modes in thick L-shaped laminates with different lay-ups. Although, experimental studies are limited to specific geometries, boundary conditions and lay-ups, they are essential in validating numerical models used throughout the design process. In the present paper we use the experimental results of Sun et al. [9] as a reference to compare our simulation results, with the ultimate goal of predicting accurate failure loads, modes and locations in curved laminates.

Most et al. [3] highlighted the importance of accurately quantifying the stress distribution when analysing debonding failure in thick curved laminates, and various methods have been suggested in the literature to cal-

*Corresponding author

Email address: thclaudi@ethz.ch (C. Thurnherr)

culate stresses in curved laminates. Three-dimensional (3D) finite element models are of course the most natural option, but their computational cost is prohibitive for iterative design studies as many elements are required through the thickness of each layer to obtain accurate stress results [3]. Computationally more efficient models include closed-form solutions based on first-order shear deformation theory [10, 11], but these models do not account for higher-order terms and are therefore less accurate for thicker laminates or when layerwise anisotropy of the laminate increases [12]. Kress et al. [13] suggested a model to analyze radial stresses in relatively thick curved laminates, and this model was later improved by Roos and Kress [14] to account for interlaminar shear stresses.

In a recent publication, the present authors developed a higher-order beam model from the Hellinger-Reissner mixed variational principle for stress analysis in curved multilayered beams of arbitrary thickness [15]. The model was validated using a high-fidelity 3D finite element model and the hoop stress, interlaminar shear stress and radial stress were all predicted accurately for different loading conditions and lay-ups. Furthermore, by solving the governing differential equations in the strong form using the pseudo-spectral differential quadrature method [16], even localized stress fields and boundary layers towards supported edges were captured. As this beam model is an equivalent single-layer model, the computational expense is independent of the number of layers and is therefore suited for computationally efficient analysis.

The objective of this paper is to use this mixed higher-order beam model for the analysis of failure initiation in curved multi-layered beams with the ultimate goal of predicting accurate failure loads, failure locations and failure modes. Furthermore, our aim is to provide physical insight into the critical stress component that drives the failure initiation event and show how the critical stress changes with varying laminate thickness and boundary conditions. Section 2 provides a brief overview of the higher-order beam model and the failure criteria, such as the maximum stress, Tsai-Hill, interlaminar failure criteria and the failure index, which are used to numerically predict the onset of damage. The experimental benchmark [9] is explained in Section 3.1 and then compared with the higher-order beam model in Section 3.2. Subsequently, failure maps are presented showing the most critical stress component throughout the cross-section of the curved laminate. Finally, Sections 4 and 5 parametrically study the influence of laminate thickness and boundary condition on damage initiation.

2. Higher-order beam model for stress prediction

This section provides a brief overview of the mixed variational higher-order beam model used throughout this paper. The detailed derivation and verification of the model can be found in [15].

The model considers a curved laminated beam element with constant midplane radius of curvature R and thickness t as shown in figure 1. This beam is referred to in a two-dimensional cylindrical co-ordinate system with co-ordinate r describing the radial direction and co-ordinate φ describing the circumferential direction.

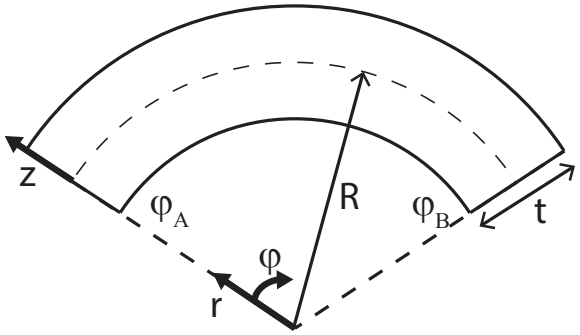

Figure 1: Definition of a curved beam element [15].

Figure 2 shows the loads acting on this curved beam, namely prescribed shear and radial tractions $\hat{T}_t$ and $\hat{P}_t$ on the top surface and $\hat{T}_b$ and $\hat{P}_b$ on the bottom surface, which may vary with the angular co-ordinate φ. Additionally, the beam may be loaded by a hoop stress σ_φ or hoop displacement u_φ, and/or a transverse shear stress $\sigma_{r\varphi}$ or transverse displacement u_r at the two ends φ_A and φ_B.

Figure 3 shows the numbering convention for the composite layup with N layers. The positions of the layers are numbered beginning with t_0 at the bottom ($z = -t/2$) and ending at the top with t_N ($z = t/2$). The kth layer is thus defined on the interval $[t_{k-1}, t_k]$. Throughout the rest of the paper the midplane of the beam is assumed as the reference surface of the equivalent single layer.

As a starting assumption, the hoop stress σ_φ is formulated as a series of higher-order stress resultants multiplied by Legendre polynomials,

$$\sigma_\varphi = \bar{Q}^{(k)}\epsilon_\varphi^G = \bar{Q}^{(k)}\frac{1}{z+R}\mathbf{f}^T(z)\mathbf{s}\mathcal{F} = \bar{Q}^{(k)}\frac{1}{r}\mathbf{f}^T(r-R)\mathbf{s}\mathcal{F} \tag{1}$$

where $\bar{Q}^{(k)}$ is the reduced stiffness matrix based on either a plane-strain or plane-stress assumption in the ra-

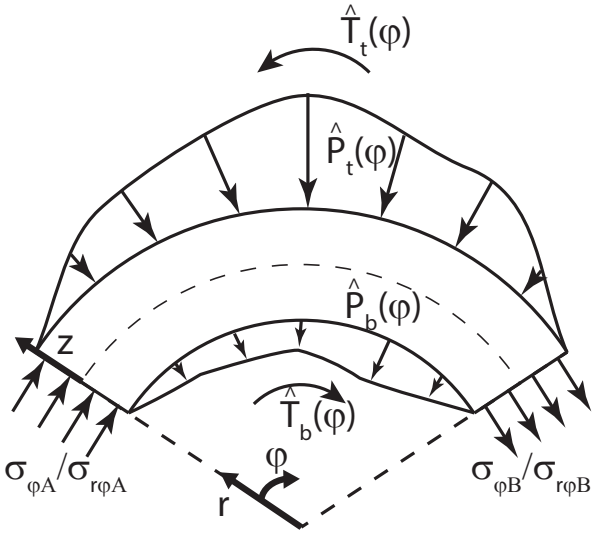

Figure 2: Loads on the beam element [15].

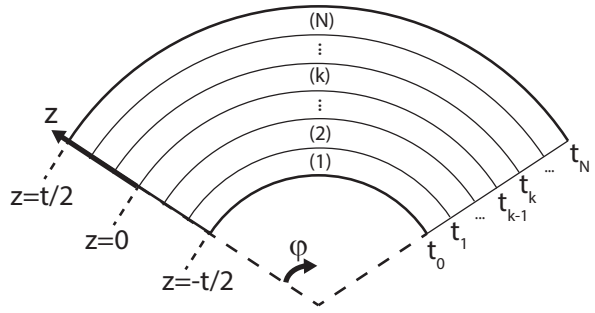

Figure 3: Layerwise notation [15].

dial direction, $\mathbf{f}$ is an array of Legendre polynomials, and $\mathcal{F}$ is an array of stress resultants. In this sense, the number of Legendre polynomials in $\mathbf{f}$ determines the fidelity of the model, and the higher the modeling order, the greater the number of higher-order effects that can be accounted for. Model assumptions for the through-thickness shear and normal stresses are derived by integrating the hoop stress of Eq. (1) in Cauchy's polar equilibrium equations in the absence of body forces [17]. Namely,

$$\sigma_{r\varphi,r} + \frac{1}{r}\left(2\sigma_{r\varphi} + \sigma_{\varphi,\varphi}\right) = 0 \tag{2}$$

and

$$\sigma_{r,r} + \frac{1}{r}\left(\sigma_r - \sigma_\varphi + \sigma_{r\varphi,\varphi}\right) = 0. \tag{3}$$

As a result, the hoop stress and transverse stress fields are based on the same set of variables, considerably reducing the computational effort. These stress assumptions are used within the principle of minimum complementary energy to derive a set of 2D stress-displacement relations. To guarantee interlaminar continuity of the transverse stresses, the equivalent single-layer form of Cauchy's equilibrium equations [15], namely

$$\begin{aligned}&\left(1+\tfrac{t}{2R}\right)\left(R+\tfrac{t}{2}\right)\hat{T}_t - \left(1-\tfrac{t}{2R}\right)\left(R-\tfrac{t}{2}\right)\hat{T}_b \\ &+\tfrac{1}{R}M_{\varphi,\varphi} + N_{\varphi,\varphi} = 0\end{aligned} \tag{4}$$

and

$$\begin{aligned}&\left(\tfrac{t}{2}+R\right)\hat{P}_t - \left(-\tfrac{t}{2}+R\right)\hat{P}_b - N_\varphi \\ &+\tfrac{1}{R}\left[\tfrac{t}{2}\left\{\left(R+\tfrac{t}{2}\right)\hat{T}_{t,\varphi} + \left(R-\tfrac{t}{2}\right)\hat{T}_{b,\varphi}\right\} + M_{\varphi,\varphi\varphi}\right] = 0\end{aligned} \tag{5}$$

need to be enforced in the minimisation of the complementary energy. These two equations are enforced via two Lagrange multipliers, which correspond to displacements in the radial and hoop direction, respectively, such that a Hellinger-Reissner-type functional is obtained. To obtain the governing equations and boundary conditions of the system, the first variation of the potential energy functional Π:

$$\Pi(\lambda,\mathcal{F}) = \Pi_r(\mathcal{F}) + \Pi_\varphi(\mathcal{F}) + \Pi_{r\varphi}(\mathcal{F}) + \Pi_\Gamma(\mathcal{F}) + \Pi_\lambda(\lambda,\mathcal{F}) \tag{6}$$

must vanish. Hence,

$$\delta\Pi = 0 \tag{7}$$

where Π_r, Π_φ and $\Pi_{r\varphi}$ denote the complementary strain energies of the stress terms in the r-, φ- and $r\varphi$-directions, respectively, Π_Γ represents the potential energy due to the loads acting on boundary $\Gamma = (z \times \varphi_A) \cup$

$(z \times \varphi_B)$, and Π_λ is the Lagrange multiplier potential associated with the equivalent single-layer equilibrium equations.

The resulting governing equations are of the form of an ordinary second order differential equation, which can be solved with little numerical effort. To solve the governing equations and the related boundary conditions in their strong form the differential quadrature method (DQM) is used. It has been previously shown that DQM is an efficient strategy for solving the stretching and bending problems [18, 19] of composite laminates. In the present work the Lagrangian polynomial weighting matrix based on the non-uniform Chebychev-Gauss-Lobatto grid is used [16] which provides excellent numerical convergence and stability properties. By replacing all the derivatives with the differential quadrature weighting matrix, the differential equations are transformed into a system of linear algebraic equations corresponding to the grid points within the Chebychev-Gauss-Lobatto grid.

2.1. Failure criteria

The stress results of the higher-order beam model are used to evaluate different failure criteria which are then compared to experimental data in the literature. A number of different failure criteria are presented herein, but in all cases the computed stresses are compared to known material strengths and damage is assumed to initiate when the criterion exceeds the value of unity.

The quadratic failure index F which includes the quadratic terms of all three stress components can be defined based on a general strength tensor theory proposed by Goldenblat and Kopnov [20]:

$$F = \left(\frac{\sigma_\varphi}{X_T}\right)^2 + \left(\frac{\sigma_r}{Y_T}\right)^2 + \left(\frac{\sigma_{r\varphi}}{S}\right)^2 \tag{8}$$

where X_T is the material tensile strength in the hoop direction, Y_T is the tensile strength in the radial direction and S is the shear strength. The failure index can be used to indicate the location where the three stress components combine in the most deleterious way. However, the quadratic failure criterion does not provide information about which specific stress component is the most critical.

Another common failure criterion is based on finding the worst stress component. Hereby, the material strengths are individually compared to the acting stresses, and if a particular material strength is exceeded then failure is expected to occur. So failure occurs when,

$$\begin{aligned} \sigma_\varphi &\geq X_t \text{ or} \\ \sigma_r &\geq Y_t \text{ or} \\ \sigma_{r\varphi} &\geq S. \end{aligned} \tag{9}$$

Note that compared to the quadratic failure criterion, the maximum stress criterion is non-interactive as the effects of a combined stress state are ignored.

The quadratic failure criterion can be modified along the lines of the maximum stress criterion to provide information about the dominant stress component within the structure. This information is useful as it facilitates plotting of failure maps that show the most critical stress component in each location of the beam cross section. In all failure maps plotted herein, a colour code is implemented to indicate the critical stress component.

Hence, if the hoop stress is the critical stress component then the following condition

$$\left(\frac{\sigma_\varphi}{X_T}\right)^2 \geq max\left(\left(\frac{\sigma_r}{Y_T}\right)^2, \left(\frac{\sigma_{r\varphi}}{S}\right)^2\right) \tag{10}$$

is fulfilled and the location within structure is shaded blue.

If the radial stress is critical then the condition

$$\left(\frac{\sigma_r}{Y_T}\right)^2 \geq max\left(\left(\frac{\sigma_\varphi}{X_T}\right)^2, \left(\frac{\sigma_{r\varphi}}{S}\right)^2\right) \tag{11}$$

must be fulfilled and the location is marked in red.

Finally, if the shear stress is critical the condition

$$\left(\frac{\sigma_{r\varphi}}{S}\right)^2 \geq max\left(\left(\frac{\sigma_r}{Y_T}\right)^2, \left(\frac{\sigma_\varphi}{X_T}\right)^2\right) \tag{12}$$

must be fulfilled and the location is marked in green.

For comparison purposes, the popular Tsai-Hill failure criterion [21, 22]

$$F_{TH} = \left(\frac{\sigma_\varphi}{X_T}\right)^2 + \left(\frac{\sigma_{r\varphi}}{S}\right)^2 \tag{13}$$

which does not consider the radial stress component, is also used.

Further, we use the interlaminar failure criterion proposed by Chang and Springer which is only valid at layer interfaces and does not include the hoop stress [23]

$$F_C = \left(\frac{\sigma_r}{Y_T}\right)^2 + \left(\frac{\sigma_{r\varphi}}{S}\right)^2. \tag{14}$$

3. Experimental validation of damage onset in a curved laminate

The higher-order beam model and failure criteria introduced in Section 2 are used to predict the onset of in-plane and debonding failure in curved laminates, and to provide physical insight into the dominant stress components that drive the failure event. To do this, a sample configuration from an experimental test found in the literature [9] is taken as a benchmark.

3.1. Experimental example for comparison

The experimental study by Sun et al. [9] investigates L-shaped laminates, with a curved portion connecting two straight sections. As failure occured in the curved sections of these L-shaped laminates the results are a suitable benchmark to compare with the higher-order beam model. The load case is modeled as a singly curved laminate with constant curvature and an opening angle of 90° subject to a shear force and a bending moment at one of its ends.

Sun et al. [9] tested L-shaped specimens with three different lay-ups and thicknesses. The first two lay-ups are taken as a reference for the present simulation, as the first lay-up exhibited failure by in-plane matrix cracking and the second lay-up failed via delamination. Figure 4 shows a microscopic photograph of the initial matrix cracks in the first sample configuration. Figure 5 shows a microscopic photograph of the delamination failure along 0°/90° interfaces in the second sample configuration. These two lay-ups comprise a graphite/epoxy prepreg system with mechanical properties listed in table 1, material strengths listed in table 2, and stacking sequences given in table 3.

Table 1: Material properties in [Msi] (GPa) and [inch] (mm) [9], the original research paper used imperial units which are converted to SI units in parentheses.

Material	E_1	E_2	G_{12}
Graphite	20 (137.9)	1.45 (10)	0.76 (5.2)
	ν_{12}	*Thickness*	
	0.3	0.005 (0.127)	

Table 2: Material strength in [ksi] (MPa)[9].

Material	*X*	*Y*	*S*
Graphite	310 (2137.4)	8.20 (56.54)	18 (124.1)

Figure 6 shows the experimental set-up used in [9] and the corresponding transformation to the boundary

Table 3: Stacking sequences [9].

Lay-up	Stacking sequence	Number of plies
1	$[90, 0_3, 90_2, 0_3, 90]_s$	20
2	$[90_3, 0, 90_3, 0, 90, 0]_s$	20

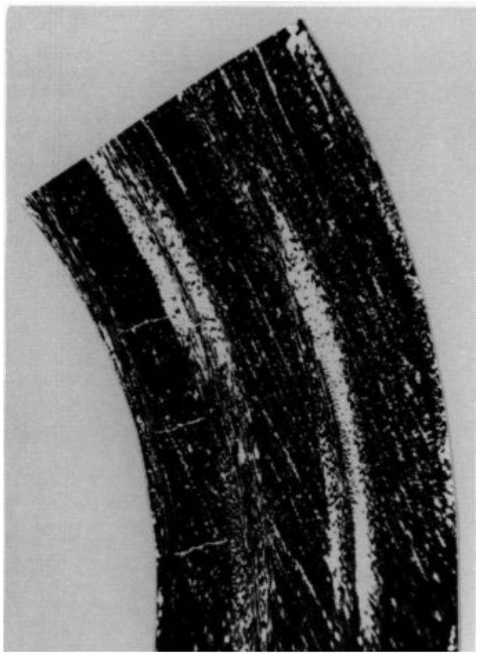

Figure 4: Microscope photograph of lay-up 1 specimen showing initial radial cracks, taken from [9].

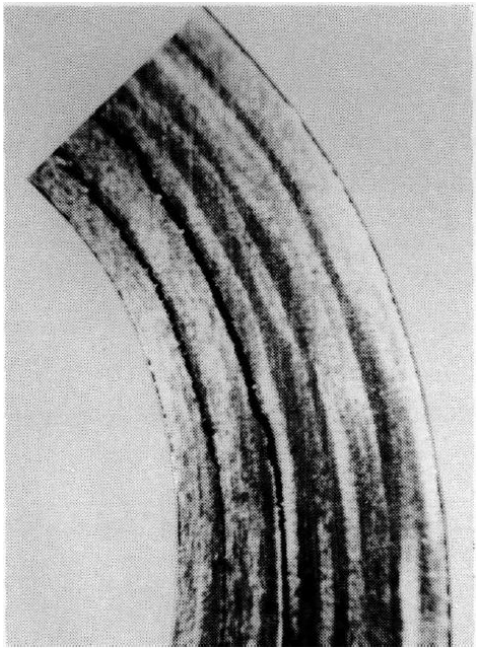

Figure 5: Microscope photograph of lay-up 2 specimen showing delamination along $0°/90°$ interfaces, taken from [24].

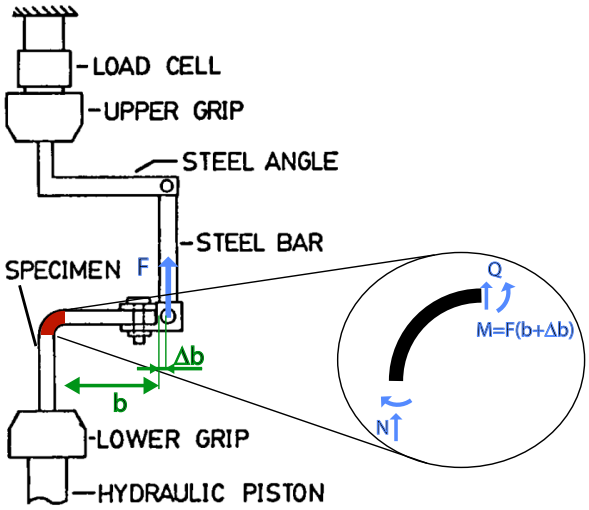

Figure 6: Experimental set-up as reported in [9] and the transformation to the boundary condition applied only to the curved element.

conditions used in the present simulation. The experimental sample is clamped at one leg and a perpendicular force is applied to the other leg. Hence, the curved part of the laminate is loaded via a bending moment that equals the applied force times the lever arm b. As the exact length of the lever arm is uncertain, it is assumed herein that the lever arm is equal to the length of the leg, i.e. 2.72 inch. In the actual experimental setup shown in Figure 6 the uncertainty in the lever arm length is denoted by a small unknown distance Δb.

Sun et al. also conducted a finite element analysis using a plane-strain FE model with four-node quadrilateral elements and three elements per ply. Their analysis was conducted with a load of 100 lb/in (which does not correspond to the experimental failure load) with the goal of qualitatively explaining the observed failures.

3.2. Numerical failure investigation

Figure 6 shows the loading of the L-shaped samples that were tested in the experiments by Sun et al. In the present simulation only the curved part of the laminate is considered. In the numerical simulation the experimental loading is reproduced by translating the vertical force F acting at the end of the horizontal leg to the end of the curved section. Hence, one end of the curved section is loaded by a vertical shear force $Q = F$ and a bending moment $M = F(b + \Delta b)$ where Δb denotes the uncertainty in the lever arm in the experimental set-up, see also Figure 6. Additionally, at the constrained end of the curved beam, φ_A, the vertically applied force F is reacted by a normal force N and a bending moment M.

To replicate the experiments tests conducted by Sun et al. [9], one end, φ_A, is clamped and a bending moment $\hat{M}$ and a shear force $\hat{Q}$ are applied on the other end, φ_B, of a curved beam with inner radius 0.18 inch, opening angle $\psi_0 = \pi/2$ and an overall thickness of 0.1 inch as shown in figure 7.

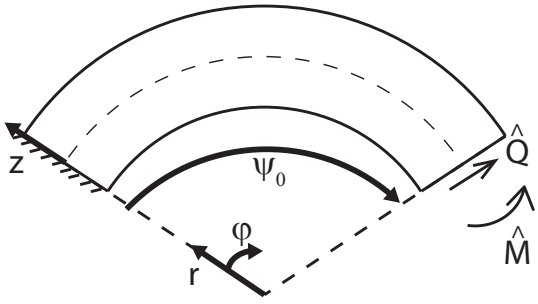

Figure 7: Definition of the boundary conditions.

To validate the stress results of the Hellinger-Reissner beam model we conducted a finite element analysis of the entire L-shaped sample including the two protruding legs. As is the case in the experiments, the sample was clamped at the end of the vertical leg and a verti-

cal force was applied at the end of the horizontal leg. The model was implemented as a plane strain model in *ANSYS classic 14.5* using an 8-node PLANE183 element with 4 elements per layer and hence 80 elements through the thickness, 100 elements in the hoop direction, and 400 elements along the in-plane direction of each leg.

Lay-up 1

In the experimental study an average initial failure load of 33 $[lb/in]$ was found for lay-up 1. Therefore, the moment applied in the higher-order beam model is set equal to the failure load times the lever arm of 2.72 inch, i.e. $\Delta b = 0$ inch. With this approach a quantitative comparison with the experiments is also possible: if the failure criterion is equal to unity, then the experimental and numerical failure load match identically.

Figure 8 shows the stress distribution in the curved laminate for lay-up 1 calculated with the Hellinger-Reissner model. The solution converges for modeling order three, i.e. including up to a third-order Legendre polynomial, and nine Chebychev-Gauss-Lobatto grid points. As expected the highest hoop stress is observed in the layers with the fibers aligned in the hoop direction. Due to the relatively large thickness of the beam, significant radial stresses develop and these influence the failure behavior. The stress distribution obtained with the Hellinger-Reissner model qualitatively correlates with the FEM results reported in [9]. Figure 9 shows the comparison between the FE results obtained by Sun et al., the Hellinger-Reissner beam model, and the *ANSYS* FE model results, where a denotes the inner radius of the curved laminate. The Hellinger-Reissner model and the *ANSYS* FE model match very well and the curves are in fact graphically indistinguishable. However, the results obtained from these two models are about 6% smaller for the hoop stress and 8% smaller for the radial stress when compared to Sun et al.'s original FE model. In the beginning of this section we described an underlying uncertainty in the exact length of the lever arm, and this may in fact explain the discrepancy between our results and the results reported by Sun et al.

Figure 10 shows the maximum stress failure criterion for the three stress components. The highest values are observed in the 0° layers with the smallest radius of curvature. The maximum stress criterion predicts in-plane matrix failure in these layers which agrees with the experiments conducted by Sun et al. [9]. The largest hoop stress to strength ratio is 1.09 in the simulation, hence it agrees well with the initial failure load measured in the experiments. Furthermore, the maximum radial stress

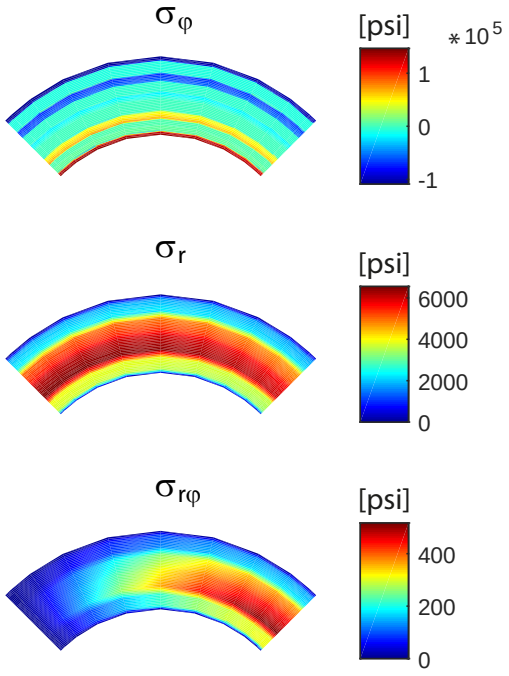

Figure 8: Stress distribution of σ_φ, $\sigma_{r\varphi}$, and σ_r for $n = 3$ (order of through-thickness Legendre polynomial) and lay-up 1.

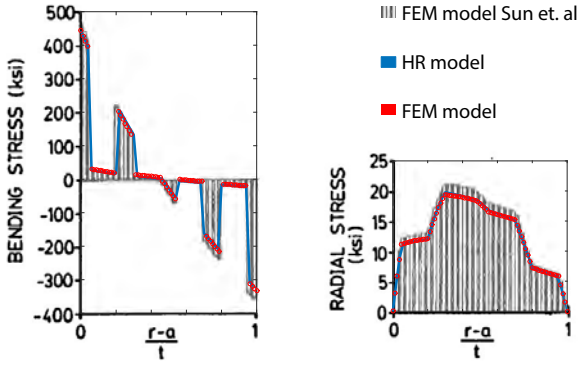

Figure 9: Comparison of stress distribution of σ_φ and σ_r in lay-up 1 obtained with the FEM model by Sun et al. [9], the Hellinger-Reissner model for $n = 3$, and our FEM model at $\varphi = 25°$.

to strength ratio reaches a maximum of 0.79 which suggests that this stress component may also be an important driver in damage initiation. However, the greatest radial stress occurs in the middle of the beam and hence in a different location than the maximum hoop stress. Finally, for lay-up 1 the effect of the transverse shear stress is negligible.

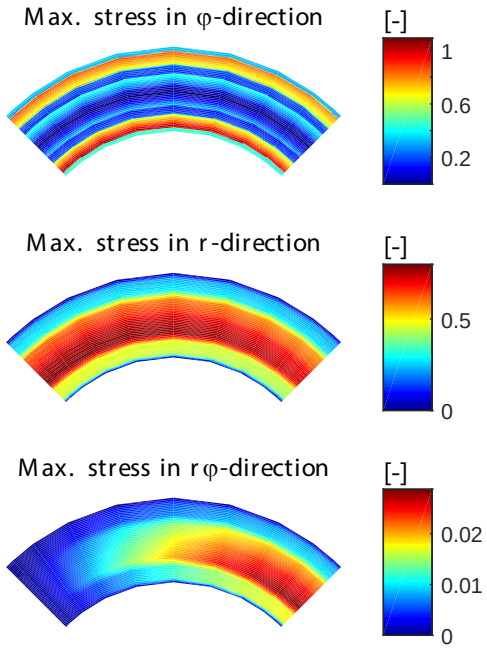

Figure 10: Max. stress yield criterion for hoop, shear, and radial stress for lay-up 1.

Figure 11 shows the Tsai-Hill, interlaminar failure criterion and failure index. The Tsai-Hill criterion predicts almost the same failure load (max. value 1.19) and location as found in the experiments and also corroborates the findings for the maximum stress criterion. The interlaminar failure criterion shows maximum values of around 0.64 which is therefore not close to inducing failure initiation. Finally, the failure index, which accounts for intra- and interlaminar components simultaneously, also indicates that failure initiates in the 0° layer with the smallest radius of curvature although at a load slightly lower than observed experimentally (the failure criterion is significantly greater than unity).

Figure 12 shows the failure map for lay-up 1 and suggests that the hoop stress is critical for the outer layers, whereas the radial stress is critical for the inner layers. This was also observed in the experiments where in-plane matrix failure was reported as the initial failure

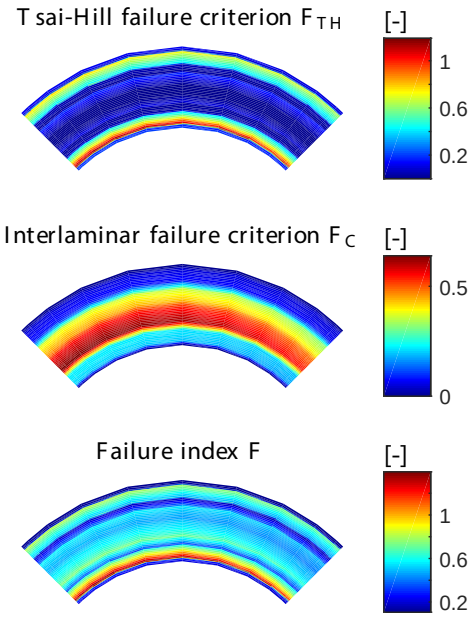

Figure 11: Tsai-Hill failure criterion, interlaminar failure criterion and failure index for lay-up 1.

event, followed by debonding in the middle of the beam as loading continued.

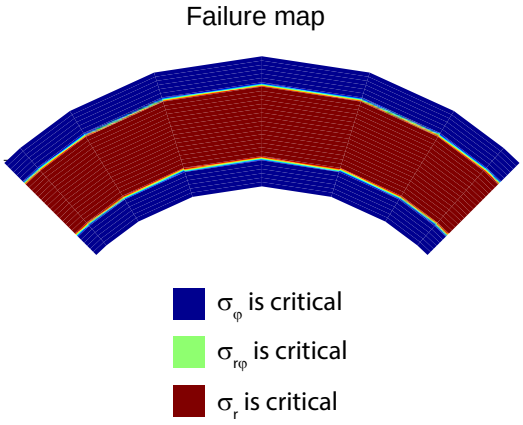

Figure 12: Failure map for lay-up 1.

Lay-up 2

For lay-up 2 the experimentally found initial failure load was 44 $[lb/in]$ and a corresponding moment was applied in the higher-order beam model. Figure 13 shows the stress distribution in the curved laminate for

lay-up 2 using a modeling order of three (third-order Legendre polynomial), and nine grid points along the arc-length of the beam. The greatest hoop stress again occurs in the layers with fibers oriented in the hoop direction. In this case, significant radial stresses are observed in the middle of the laminate, whereas the transverse shear stresses are more than one order of magnitude smaller and hence do not influence the failure behavior.

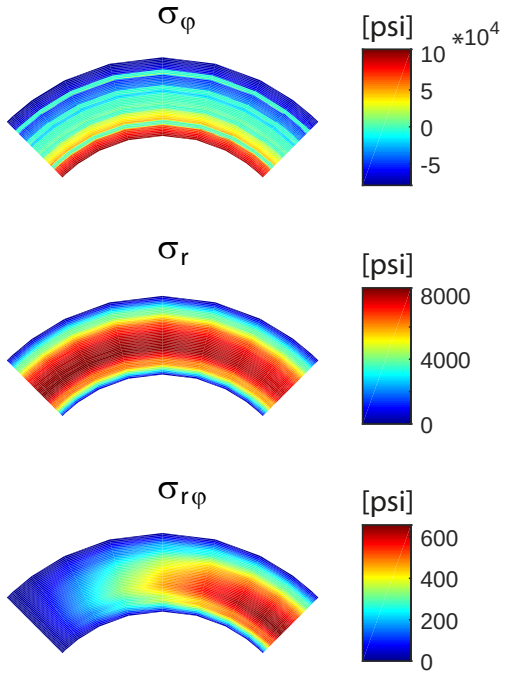

Figure 13: Stress distribution of σ_φ, $\sigma_{r\varphi}$, and σ_r for $n = 3$ and lay-up 2.

Figure 14 shows the comparison of the stress distribution calculated by the FEM model of Sun et al. [9], the *ANSYS* FEM results and the Hellinger-Reissner model obtained with a load of $100 lb/in$. As for the first lay-up, while the results correlate very well qualitatively, the stresses for the Hellinger-Reissner and *ANSYS* FE model are around 9% smaller for the hoop stress and 12% smaller for the radial stress for $\Delta b = 0$ inch. As for the previous lay-up a very good match between the Hellinger-Reissner and our *ANSYS* FEM model is obtained.

The maximum stress failure criterion in Figure 15 shows that the radial stress is the dominant factor in the failure initiation with the radial stress to strength ratio reaching a maximum value of 1.025. Compared to lay-

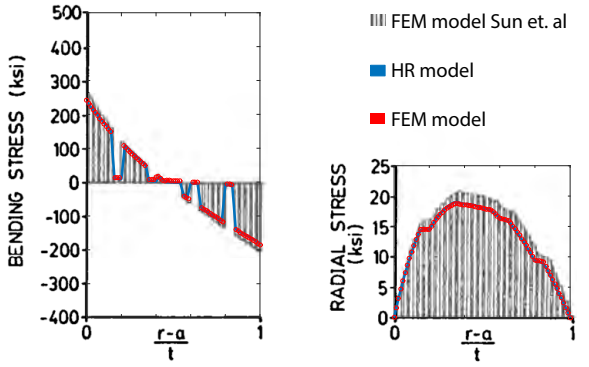

Figure 14: Comparison of stress distribution of σ_φ and σ_r in lay-up 2 obtained with the FEM model by Sun et al. [9], the Hellinger-Reissner model for $n = 3$, and our FEM model at $\varphi = 25°$.

up 1 the hoop stress to strength ratio is much smaller at 0.55. This again correlates well with the experimental findings by Sun et al. who found delamination to be the first failure in their experiments. Sun et al. found delamination between the $0°/90°$ interfaces (see Fig. 5) which is also indicated by the maximum stress criterion in the radial direction of Figure 15. The load at which failure initiates is well correlated because the model predicts a failure criterion of almost unity.

Figure 16 shows the Tsai-Hill, interlaminar failure criteria and failure index for lay-up 2. For this lay-up the Tsai-Hill criterion is much smaller than unity, whereas the interlaminar failure criterion shows values up to 1.05. Hence the higher-order beam model strongly suggests that delamination is the mode of failure as is indeed reported in [9]. Finally, the failure index which incorporates all three stress components predicts the same failure mode and location as the interlaminar failure criterion, namely interlaminar failure along the $0°/90°$ interfaces. This corresponds to the failure location and mode that Sun et al. found (see Figure 5).

Figure 17 shows the failure map for lay-up 2. It indicates that the radial stress is most critical throughout almost the entire cross-section.

The comparison of experimental results by Sun et al. [9] and the numerical predictions of the Hellinger-Reissner model correlate closely for both investigated lay-ups. When the simulation is run with an applied load corresponding to the experimental failure load, the interactive failure criteria produce values close to unity. The use of intra- and interlaminar failure criteria means that the correct failure location and mode can be predicted. In this respect, the accurate stress results of the higher-order beam model are key in accurately pre-

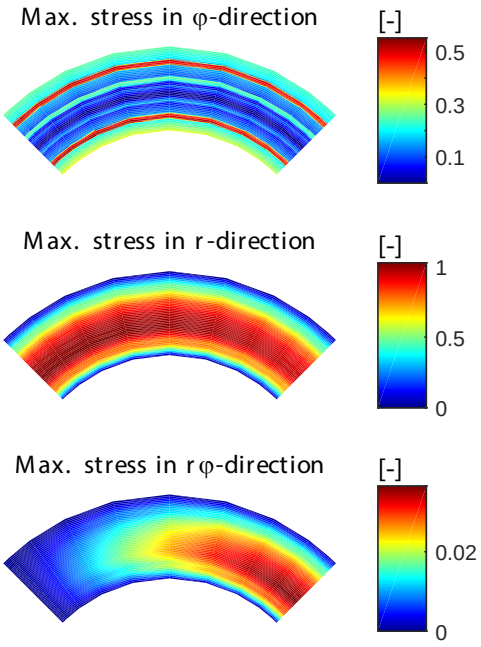

Figure 15: Max. stress yield criterion for hoop, shear, and radial stress for lay-up 2.

Figure 16: Tsai-Hill failure criterion, interlaminar failure criterion and failure index for lay-up 2.

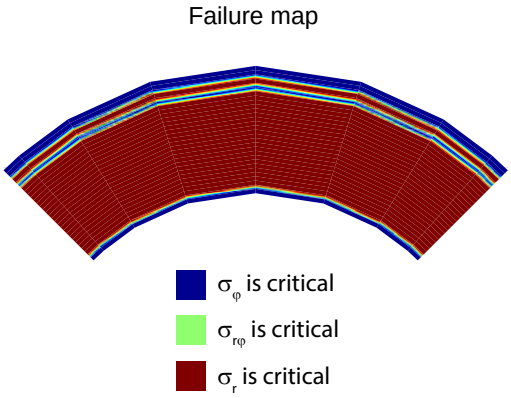

Figure 17: Failure map for lay-up 2.

dicting damage onset. Some remaining differences between the experimental and numerical results can be explained by uncertainties or variations in the stiffness and strength properties of the material, possible hoopwise thickness variations in the samples due to fabrication uncertainties, small deformations in the legs of the samples, as well as uncertainties in the clamping and the lever arm Δb which can never fully be avoided in experimental testing. Similar results are of course readily computable from a finite element model, but the computational effort using the higher-order beam model is significantly reduced as it is based on an equivalent single layer approach. As the model only requires a few seconds to run it is ideally suited as an analytical tool for iterative design studies in industry.

4. Influence of laminate thickness on the critical stress component

In this section the influence of laminate thickness on the critical stress component is investigated for a uniform lay-up with all fibers aligned along the hoop direction. In comparison to the simulations done already, we consider pure bending boundary conditions as shown in figure 18. The stress response for ten different thicknesses is computed while keeping the radius and loading constant. The thickness of the laminate is varied by increasing the number of layers in the laminate from two to 20 in two-layer increments. For each configuration i the squared stress to strength ratio of the three stress components is calculated over the beam domain

$$\left(\left(\frac{\sigma_r}{Y_T}\right)^2,\left(\frac{\sigma_\varphi}{X_T}\right)^2,\left(\frac{\sigma_{r\varphi}}{S}\right)^2\right)_i\Bigg|_{\varphi=\varphi_A,r=R-\frac{t}{2}}^{\varphi=\varphi_B,r=R+\frac{t}{2}}. \qquad (15)$$

Next, the maximum value of each squared stress to strength ratio is identified and plotted against the R/t ratio. The squared stress to strength ratios are normalized such that the highest value is unity.

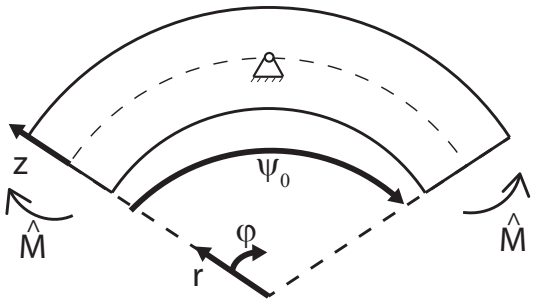

Figure 18: Definition of the pure bending boundary conditions.

Figure 19 shows that for very thin beams, which have a large R/t ratio, the hoop stress is the dominant stress field and this leads to in-plane failure. As thickness increases, the interlaminar stresses, in this case particularly the radial stress, increase in magnitude and become the dominant driver for failure initiation. Hence, the failure mode transitions from in-plane failure to delamination failure. The same phenomenon is illustrated in figures 20 and 21 where the failure criteria are plotted over the domain of the second thinnest beam and the thickest beam, respectively.

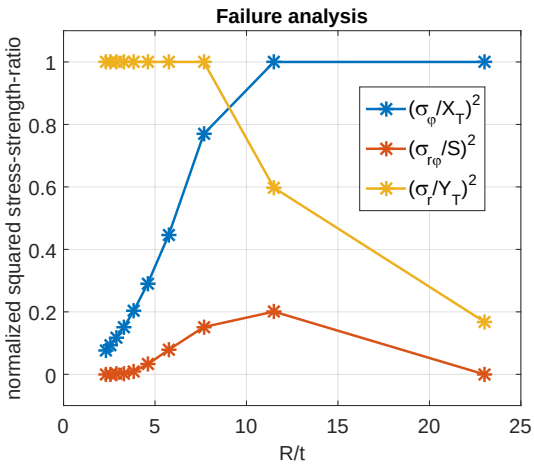

Figure 19: Failure analysis investigating the critical stress component for different laminate thickness.

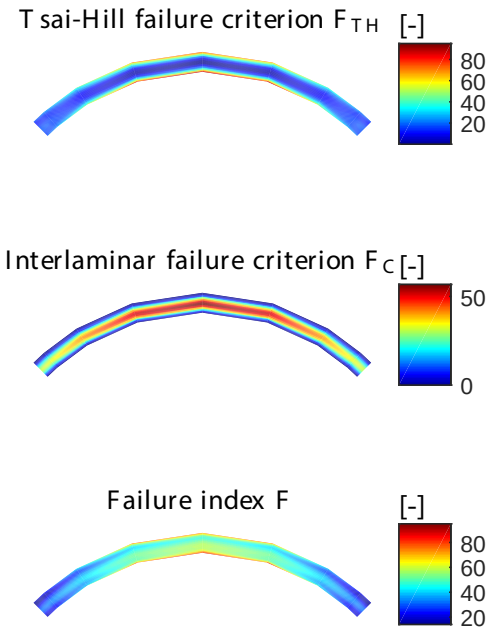

Figure 20: Failure criteria for the second thinnest beam.

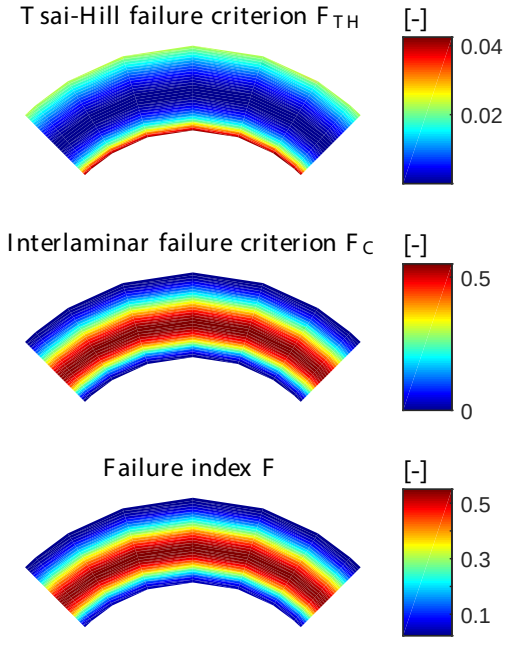

Figure 21: Failure criteria for the thickest beam.

5. Influence of clamping on critical stress component

The previous sections analysed laminates where the rotations for at least one of the ends, φ_A or φ_B, is not restricted. In these cases the critical interlaminar component is the radial stress. In this section we investigate a curved beam where the rotation at both ends is restricted. Therefore that the boundary conditions are modified as shown in figure 22. At φ_A movement of the beam is completely prevented whereas at φ_B a displacement w_{disp} is enforced. The curved laminate comprises 10 layers through the thickness, each with the fiber direction aligned in the hoop direction.

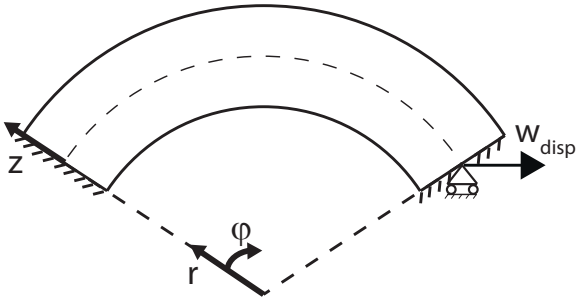

Figure 22: Clamped boundary conditions.

Figure 23 shows that in most parts of the cross-section the interlaminar shear stress is the critical stress component. Hence, for curved beams clamped at both ends the interlaminar shear stress drives debonding failure, whereas for curved beams that allow more bending rotation, the radial stress is dominant.

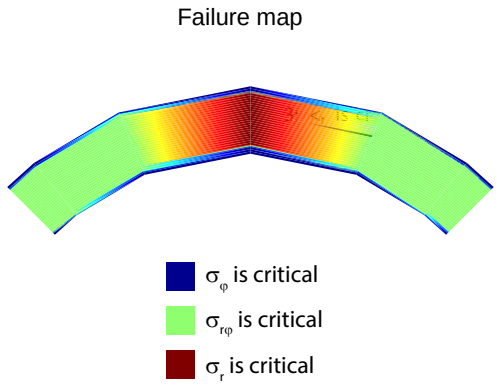

Figure 23: Failure map for clamped laminate.

Figure 24 shows the influence of beam thickness on the stresses in the fully clamped beam. The thickness is again increased by modeling beams with two to twenty layers in two-layer increments. The normalized squared stress to strength ratio is plotted for each stress component. For very thin beams the hoop stress is again critical for damage onset. As the number of layers increases, the transverse shear stress becomes the critical stress field and this leads to delamination cracks rather than in-plane failure.

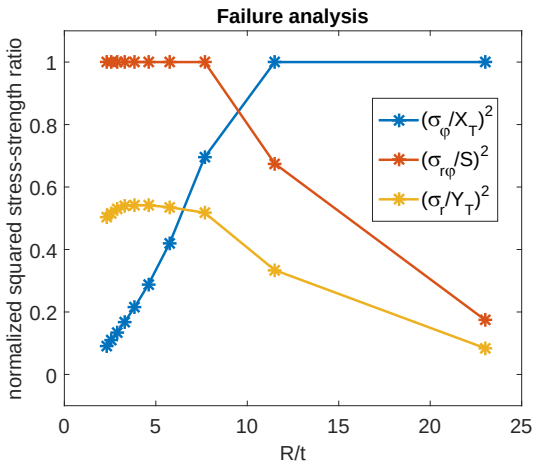

Figure 24: Failure analysis investigating the critical stress component for different R/t-ratios and clamped ends.

6. Conclusions

Damage onset in curved laminated beams can accurately be predicted using an equivalent single-layer model derived from the Hellinger-Reissner mixed variational statement. The stresses predicted with this model are used to calculate in-plane and interlaminar failure criteria and the results are compared with two different experimental tests found in the literature. The results show very good agreement between the experimental and numerical data for the damage inititation load as well as the failure mode and location. Due to the accurate three-dimensional stress fields provided by the higher-order beam model, both in-plane matrix failure and delamination initiation are predicted correctly.

The present study also highlights the importance of accurately modeling through-thickness stresses as these stresses play a key role in the failure initiation of thicker curved laminates. A parametric study showed that for very thin laminates the hoop stress is the critical stress component and causes in-plane failure initiation. However, as the thickness increases, interlaminar stresses be-

come more important and initiate delamination cracks. An extension of the study was conducted where curved laminates with two clamped ends were modeled. This study showed that for this loading condition the interlaminar shear stress is the critical interlaminar stress component, whereas for curved beams with at least one non-clamped end the radial stress is critical.

In conclusion, the presented Hellinger-Reissner model can be used alongside commonly used failure criteria to predict the onset of damage in curved laminates under applied bending moments. The model is especially attractive as it is based on an equivalent single-layer premise and therefore remains computationally efficient even for large number of layers.

Acknowledgment

The first and third authors gratefully acknowledge the support of the Swiss National Science Foundation (project no. 149200). The second and fourth authors sincerely thank the Engineering and Physical Sciences Research Council for funding through the EPSRC Centre for Doctoral Training at the Advanced Composites Centre for Innovation and Science [grant number EP/G036772/1] at the University of Bristol.

References

[1] G. Wimmer, C. Schuecker, H. E. Pettermann, Numerical simulation of delamination in laminated composite components - A combination of a strength criterion and fracture mechanics, Composites Part B: Engineering 40 (2) (2009) 158–165. doi:10.1016/j.compositesb.2008.10.006.

[2] M. R. Wisnom, M. Jones, Delamination due to interaction between curvature induced interlaminar tension and stresses at terminating plies, Composite Structures 32 (1-4) (1995) 615–620. doi:10.1016/0263-8223(95)00056-9.

[3] J. Most, D. Stegmair, D. Petry, Error estimation between simple, closed-form analytical formulae and full-scale FEM for interlaminar stress prediction in curved laminates, Composite Structures 131 (2015) 72–81. doi:10.1016/j.compstruct.2015.03.075.

[4] I. Uyar, M. A. Arca, B. Gozluklu, D. Coker, Experimental Observations of Dynamic Delamination in Curved [0] and [0/90] Composite Laminates, in: Fracture, Fatigue, Failure, and Damage Evolution, Volume 5: Proceedings of the 2014 Annual Conference on Experimental and Applied Mechanics, Vol. 5, 2015, pp. 189–196. doi:10.1007/978-3-319-06977-7.

[5] M. R. Wisnom, The role of delamination in failure of fibre-reinforced composites, Philosophical Transactions of the Royal Society A: Mathematical, Physical and Engineering Sciences 370 (1965) (2012) 1850–1870. doi:10.1098/rsta.2011.0441.

[6] G. Wimmer, W. Kitzmüller, G. Pinter, T. Wettemann, H. E. Pettermann, Computational and experimental investigation of delamination in L-shaped laminated composite components, Engineering Fracture Mechanics 76 (18) (2009) 2810–2820. doi:10.1016/j.engfracmech.2009.06.007.

[7] W. Hao, D. Ge, Y. Ma, X. Yao, Y. Shi, Experimental investigation on deformation and strength of carbon/epoxy laminated curved beams, Polymer Testing 31 (4) (2012) 520–526. doi:10.1016/j.polymertesting.2012.02.003.

[8] L. Michel, S. Garcia, C. Yao, C. Espinosa, F. Lachaud, Experimental and Numerical Investigation of Delamination in Curved-Beam Multidirectional Laminated Composite Specimen, Key Engineering Materials 577-578 (2013) 389–392. doi:10.4028/www.scientific.net/KEM.577-578.389.

[9] C. Sun, S. Kelly, Failure in Composite Angle Structures Part I: Initial Failure, Journal of Reinforced Plastics and Composites 7 (3) (1988) 220–232. doi:10.1177/073168448800700302.

[10] S. Mcrobbie, A. J. Longmuir, J. Wilcox, A. G. Gibson, H. W. Chandler, Through-thickness stress in curved laminates of single- and double-skinned construction, Composite Structures 26 (5) (1995) 339–345.

[11] R. a. Shenoi, W. Wang, Through-thickness stresses in curved composite laminates and sandwich beams, Composites Science and Technology 61 (11) (2001) 1501–1512. doi:10.1016/S0266-3538(01)00035-5.

[12] T. Kant, K. Swaminathan, Estimation of transverse/interlaminar stresses in laminated compositesa selective review and survey of current developments, Composite structures 49 (1) (2000) 65–75.

[13] G. Kress, R. Roos, M. Barbezat, C. Dransfeld, P. Ermanni, Model for interlaminar normal stress in singly curved laminates, Composite Structures 69 (4) (2005) 458–469. doi:10.1016/j.compstruct.2004.08.026.

[14] R. Roos, G. Kress, M. Barbezat, P. Ermanni, Enhanced model for interlaminar normal stress in singly curved laminates, Composite Structures 80 (3) (2007) 327–333. doi:10.1016/j.compstruct.2006.05.022.

[15] C. Thurnherr, R.M.J. Groh, P. Ermanni, P.M. Weaver, Higher-order beam model for stress predictions in curved beams made from anisotropic materials, International Journal of Solids and Structures 97-98 (2016) 16–28. doi:10.1016/j.ijsolstr.2016.08.004.

[16] C. Shu, Differential Quadrature and Its Application in Engineering, Springer, London, 2000.

[17] J. Reddy, Theory and Analysis of Elastic Plates and Shells, 2nd Edition, CRC Press, New York, 2007.

[18] R.M.J. Groh, P.M. Weaver, S.C. White, G. Raju, Z. Wu, A 2D equivalent single-layer formulation for the effect of transverse shear on laminated plates with curvilinear fibres, Composite Structures 100 (2013) 464–478. doi:10.1016/j.compstruct.2013.01.014.

[19] R.M.J. Groh and P.M. Weaver, A computationally efficient 2D model for inherently equilibrated 3D stress predictions in heterogeneous laminated plates. Part II: Model validation, Composite Structures 156 (2016) 186–217, Special Issue 70th Anniversary of Professor J. N. Reddy . doi:10.1016/j.compstruct.2015.11.078.

[20] I. Goldenblat, A. Kopnov, Strength of glass-reinforced plastics in the complex stress state, Mekhanika Polimerov 1 (2) (1965) 70–78.

[21] S. Tsai, Fundamental Aspects of Fiber Reinforced Plastic Composites, Wiley Interscience, New York, 1968.

[22] R. Hill, The Mathematical Theory of Plasticity, Oxford University Press, London, 1950.

[23] F.-K. Chang, G. S. Springer, The Strengths of Fiber Reinforced Composite Bends, Journal of Composite Materials 20 (1) (1986) 30–45. doi:10.1177/002199838602000103.

[24] C. Sun, S. Kelly, Failure in Composite Angle Structures Part II: Onset of Delamination, Journal of Reinforced Plastics and Composites 7 (3) (1988) 233–244.